Full Length Article

Computational observation of the strengthening of Cu/TiN metal/ceramic interfaces by sub-nanometer interlayers and dopants

Abu Shama Mohammad Miraz [a], W.J. Meng [b], Bala R. Ramachandran [a], Collin D. Wick [a,*]

[a] *College of Engineering & Science, Louisiana Tech University, Ruston, LA 71272, USA*
[b] *Department of Mechanical & Industrial Engineering, Louisiana State University, Baton Rouge, LA 70803, USA*

ARTICLE INFO

ABSTRACT

First principles density functional theory calculations were used to explore the enhancement of the structural integrity of Cu/TiN metal/ceramic interfaces by substitutional doping of the interface with Ni, Zn and Sn. To evaluate the interfacial strength, energy barriers to shear displacement and maximum tensile stress before fracture were calculated. Enthalpy of mixing dictated that Sn was not energetically suitable for doping at the interface, whereas both Ni and Zn were. Ni segregated at the interface forming sub-nanometer interlayers between Cu and TiN, whereas Zn formed a solid solution with Cu. While Zn-doping increased the resistance to shear, it led to a weakening of tensile strength. Ni interlayers increased both the shear and tensile strength to a significant degree coinciding with an increase in electron density between the layers. Using analysis form their partial density of states, Ni interlayers were found to accept more electrons from interfacial Ti into their more compact 3*d*-orbitals than Cu, which accepted more into available 4*s*-orbitals. Zn doping increased resistance to shear due to its lower electronegativity than Cu, causing interfacial Zn to have a more positive charge, which also raised the barrier to shear when in close contact with positively charged interfacial Ti atoms.

1. Introduction

In many components and systems, thin layers of metals and ceramics are selectively combined to achieve customized structural, chemical, electrical and magnetic properties, conforming to the requirements of their respective technological applications [1–4]. Such applications include functional components like sensors used in electronic devices [5]; mechanical and structural parts such as gears, valve seats and guides used in aero-engines, gas turbines, automobiles and aerospace structures [6–9]; electrodes for fuel cells [10]; machining and cutting tools, etc. [11–14]. Since the mechanical response of an entire composite system is highly influenced by the characteristics of the interfacial region, strong adhesion and structural integrity at the interface is key to the long-lasting utility of components with such composites [3,15–17]. Hence, efforts aimed at efficient design of highly durable metal/ceramic composites largely comprise of promoting adhesion and resistance to shear at the interfacial region.

Many metal/ceramic interfaces have been investigated by means of experimental and computational methods [18–32]. In particular, transition metal nitrides such as TiN, have been established as a popular thin film coating material due to their high hardness, thermal stability, and

corrosion resistance [33,34]. Such properties also qualify TiN as a diffusion barrier for Cu metallization in the Si-based microelectronic circuits, where TiN is sandwiched between Cu and a Si substrate [22,35]. In many cases, thin metal interlayers, such as Ti, have also been deposited between TiN and the substrate to impede crack propagation at the coating/substrate interface [36–38]. In both forms (metal/ceramic/substrate and ceramic/metal/substrate), the overall integrity of the multilayered structure is influenced by the adhesive strength of the metal/ceramic interface. However, promoting adhesion in metal/TiN interfaces, such as Cu/TiN, remains a challenge that requires novel concepts to be adopted.

One such concept involves 'doping' the system with common alloying elements of the host metal to enhance mechanical properties. Such concepts have guided the development of high entropy alloys in which multiple metal components are present at comparable concentrations [39,40]. For metal/ceramic interfacial systems, the 'doping' concept has been studied only for a few cases, such as for Ti/TiN [41–43], Al/Ti(N,C) [44–46], Ni/Ni₃Al [47–49], Nb/Al₂O₃ [50], and Ni/YSZ(1 1 1) [51]. Previously, we investigated the strengthening effects of dopant elements Al, Cr, and V on coherent Ti/TiN interfaces [41]. A general correlation was found between higher shear strength and the concentration of Al

* Corresponding author.

dopant atoms at the Ti/TiN interface, while the enthalpy of mixing of Cr and V in Ti proved to be positive. Cu/TiN semi-coherent interfaces are characterized by a weak interfacial strength as compared to many other metal/TiN interfaces, with a shear strength below 5 MPa [52]. Investigating how interfacial properties can be improved with doping would be beneficial to the utility of Cu/TiN interfaces in their applications and yield information for a more general approach towards engineering the mechanical integrity of metal/ceramic interfaces.

A systematic design of strong metal/ceramic interfaces requires an atomic-level understanding of the local interactions and geometries in relation to the mechanical strength. Experimental techniques for gauging mechanical properties of interfaces involves various forms of mechanical loading, leading to deformation or fracture of the interfacial region [53,54]. The availability of reliable DFT functionals coupled with modern high-performance computing resources and robust algorithms make it possible and efficient to apply predictive computational studies based on first principles methods to complex materials systems such as metal/ceramic interfaces. We have previously carried out such computational investigation of the energetics and the shear strength of clean Cu/TiN systems and found, in agreement to the experimental results, that these interfaces exhibit low interfacial strength [27,55]. Computationally developed doping strategies to strengthen such a weak interface, if found, may well be expanded to other weak interfaces with different materials. Moreover, common trends for a wider choice of materials may be inferred by considering Cu/TiN as a prototype for fcc metal/TiN interfaces.

In this work, we perform substitutional doping in the most stable Cu(1 1 1)/TiN(1 1 1) semi-coherent interfacial systems with Ni, Zn and Sn, three common alloying elements of Cu. The shear and tensile strengths of the interface were quantified with generalized stacking fault energies (GSFE), work of adhesion, and tensile stress-strain relationships, while the effect of doping was analyzed using the charge density and the density of states at the interfaces.

2. Methodology

DFT calculations were performed using the Vienna Ab-Initio Simulation Package (VASP) package [56]. Generalized gradient approximation proposed by Perdew, Burke and Ernzerhof (PBE) was used to estimate the exchange-correlation functional [57]. The Projector Augmented Wave (PAW) pseudopotentials were used for core electrons whereas the valence electrons were portrayed by a plane wave basis set with a cutoff energy of 400 eV [58]. A Γ-centered $2 \times 4 \times 1$ k-point mesh was used for the metal/ceramic systems with periodic boundary conditions [59]. Finer meshes and higher energy cutoffs were tested resulting in no significant changes in the cell dimensions or the energy. The inclusion of spin polarization in the elements studied had insignificant impact on relative energies in calculations such as energy of mixing and structural relaxation, so it was not considered further in this work.

2.1. Cu/TiN interfacial systems

Stable Cu/TiN bi-crystal systems with a semi-coherent interface was established in our previous work with the work of adhesion as a measure of stability [28]. The most stable orientation relation found for Cu/TiN is as follows,

$$X\|\left[11\bar{2}\right]_{Cu}\|\left[1\bar{1}0\right]_{TiN}; \ Y\|\left[1\bar{1}0\right]_{Cu}\|\left[11\bar{2}\right]_{TiN} \ \text{ and } \ Z\|[111]_{Cu}\|[111]_{TiN}.$$
(1)

This orientation relation has been experimentally observed in other reports as well [60–63]. For this work, we created Cu/TiN bi-crystal systems with the same orientation relation. The unit cell length in each planar direction of separately relaxed Cu and TiN structures are listed in Table 1. In order to create an interfacial system with minimal mismatch within a reasonable size for DFT calculations, the unit Cu

Table 1
Unit length along the planar dimensions of Cu(1 1 1) and TiN(1 1 1).

Surfaces	Planar Dimensions		Unit Length (Å)		Cu/TiN Periodic Units
	X	Y	X	Y	$(X \times Y)_{Cu}/(X \times Y)_{TiN}$
Cu(1 1 1)	$[11\bar{2}]$	$[1\bar{1}0]$	4.43	2.56	$(2 \times 2)_{Cu}/(3 \times 1)_{TiN}$
TiN(1 1 1)	$[1\bar{1}0]$	$[11\bar{2}]$	3.01	5.19	

(1 1 1) cell was replicated two times in both X and Y, while the unit TiN (1 1 1) was replicated three times in Y only. This resulted in a total of 96 atoms in twelve (1 1 1) layers for Cu and 72 atoms (36 of each species) in six (1 1 1) layers for TiN. These two systems are illustrated in Fig. 1(a) and (b), respectively, with the vertical black lines enclosing the periodic simulation cells. The small mismatch left was accommodated at the Cu-phase by stretching it in X and Y to match the dimensions of TiN-phase. As shown in Fig. 1(c), the interface was created by bringing the (1 1 1) planes of the two phases, Cu and TiN, together along the Z direction. TiN (1 1 1) has alternating layers of Ti and N in the Z-direction. As shown in our previous study, the Cu interfacing with the Ti-terminated surface of the ceramic is more stable than the N-terminated one [28]. Periodic boundary conditions were applied in all directions and a vacuum space of 15 Å was left along the Z direction to minimize the interaction of the system with its own periodic images in that direction. This creates two surfaces with vacuum, one for the metal and the other for the ceramic phase. The bi-crystal structure was then fully relaxed to obtain the minimum energy of the system.

Necessitated by their frequent occurrence in our discussion, convenient notations have been adopted for the (1 1 1) atomic layers and the planes between them in the rest of this paper. The (1 1 1) atomic layers stacked in the Z direction are denoted by M and the planes between these layers are marked by P. As shown in Fig. 1(c), the metal atomic layer nearest to the interface is denoted by M = 1, and the subsequent layers are identified with increasing numbers away from the interface. On the other hand, P = 0 is assigned for the interfacial plane where Ti atoms from the TiN phase comes in contact with the M = 1 metal atoms from the metal phase. The next plane, between M = 1 and 2 atomic layers, is indicated by P = 1, and so on.

2.2. GSFE calculations and barrier height

The GSFE of a crystal plane gives the variation in energy as the total system undergoes a rigid shear displacement at that plane from one lattice point to another equivalent lattice point. GSFE plots provide energetic guides for dislocation movement, which govern a range of mechanical properties such as shear strength [64–66]. To estimate the resistance to shear at the interfacial region, GSFE calculations were carried out for the interfacial planes. A GSFE for a given plane, P, is achieved by moving in concert all the atoms above that plane along the direction of slip, keeping all the atoms below fixed, as shown in Fig. 2(b). This displacement is performed in thirty equidistant steps along the full cell length in the slip direction, which, from our previous study, [28] is $X\|\left[11\bar{2}\right]_{Cu}$ as defined in Fig. 2. After each displacement step, the positions of the atoms were allowed to relax along the other two directions, Y and Z, and the total energy was calculated. These energies are plotted against the corresponding displacements to give the GSFE curve. The magnitude or peak of this plot gives the energy barrier for the shear displacement. GSFE plots obtained from the minimum energy path on the γ-surfaces of interfacial planes previously revealed that the chemical interface (P = 0 in Fig. 1(c)) has the lowest GSFE barrier, hence, is the weakest plane under shear loading [28]. So, increasing the barrier height at the interfacial plane (P = 0) by doping is considered important for improving interfacial shear strength.
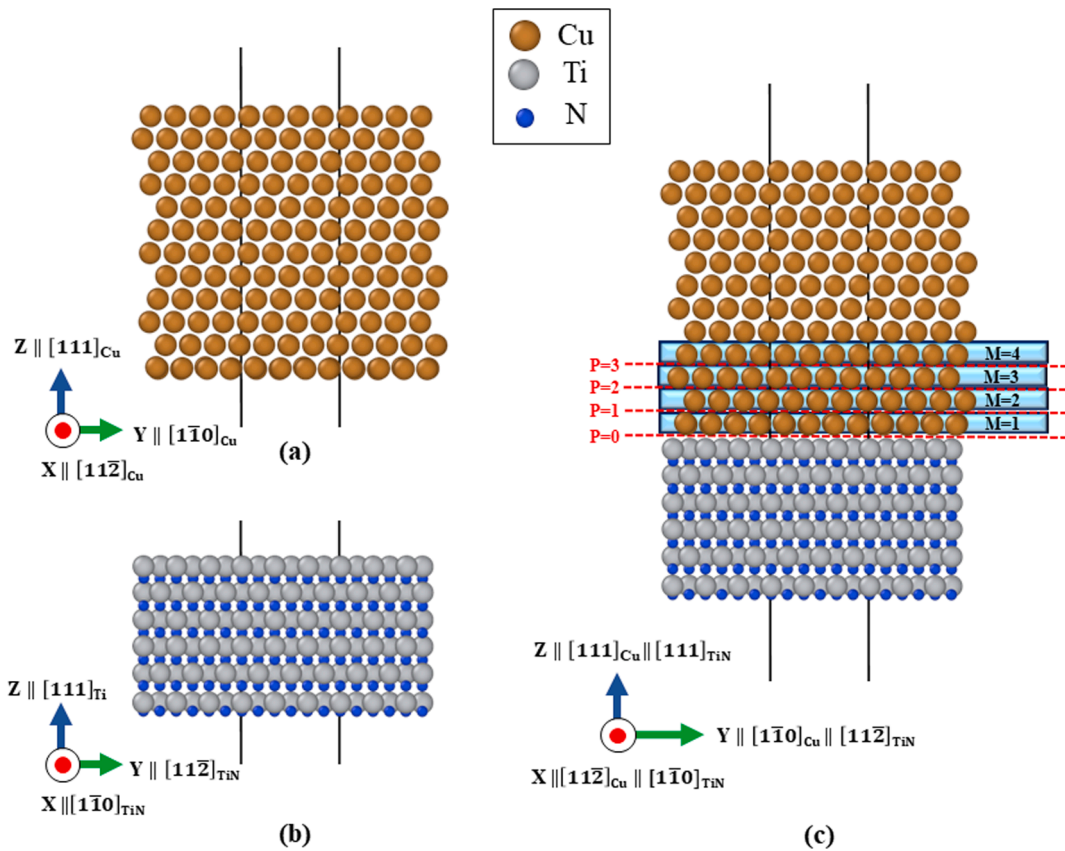
Fig. 1. (a) Cu and (b) TiN structures with crystal directions corresponding X, Y and Z axis. The vertical lines mark the boundaries of the periodic simulation cell. (c) Cu(1 1 1)/TiN(1 1 1) bilayer structure; the blue shaded boxes enclosing Cu(1 1 1) atomic layers are denoted by M and the planes between these layers indicated with broken red lines are denoted by P. (For interpretation of the references to colour in this figure legend, the reader is referred to the web version of this article.)
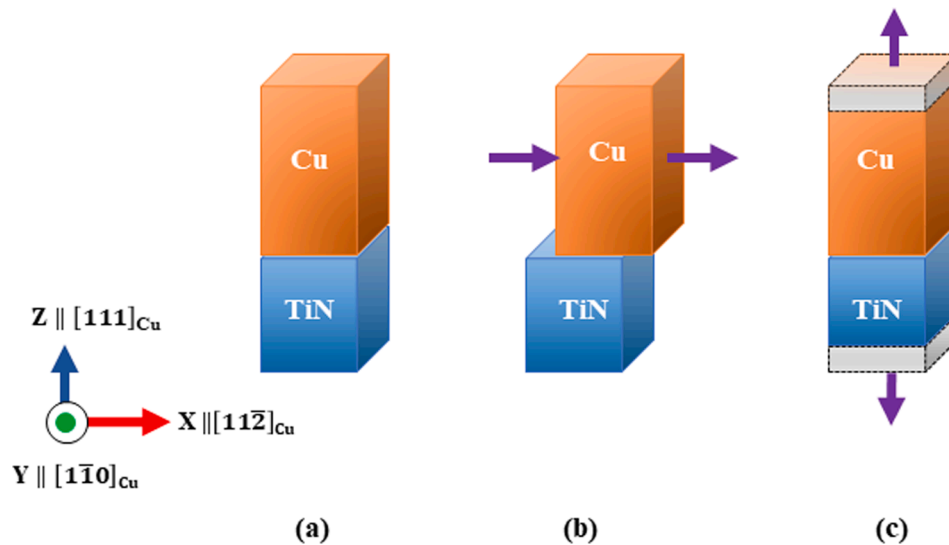

Fig. 2. (a) A schematic of the Cu/TiN system. (b) Shear displacement along X for GSFE calculations. (c) Tensile stretching along Z for tensile strength calculations with fixed top and bottom layers (shown in grey shades).

2.3. Uniaxial tensile stretching and work of adhesion

To simulate tensile stretching, the bi-crystal system was stretched in the Z direction, as shown in Fig. 2(c), in incremental steps of 0.15 Å until fracture occurred. The top two Cu layers in the Cu(1 1 1) phase and the bottom two layers of the TiN(1 1 1) phase had their Z positions kept rigid while the atoms between these layers were incrementally displaced along the Z dimension. The total displacement was kept so that the total system length increased by 0.15 Å in each step. After each displacement step, all atoms except those in the top and bottom two layers were allowed to fully relax, keeping the cell dimensions fixed. The atoms in the top and bottom two layers were allowed to relax in the X and Y dimensions, keeping their Z coordinates fixed. The Z dimension of the simulation box was readjusted to make sure at least 10 Å of vacuum was

always present. Stress was calculated by taking the difference of the energy with respect to displacement and then dividing it by area of the XY plane. If any drastic changes in the structure between two steps occurred, smaller increments were used between these two steps to observe the change in greater detail.
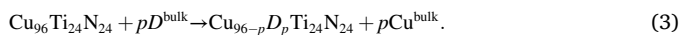
The work of adhesion (WoA), which is the energy required to separate a system into two isolated and relaxed systems, was calculated as a qualitative measure of the stability and binding. A higher WoA corresponds to stronger and energetically favorable binding [28,67]. WoA at an interface (or a plane parallel to the interface) was calculated using the following formula,

$$\text{WoA} = (E_1 + E_2 - E_{\text{total}})/A \tag{2}$$

where E_{total} is the total energy of the whole relaxed system, A is the area of the interface, E_1 and E_2 are the relaxed energies of the two isolated systems in contact with vacuum.

2.4. Stable doping configurations

Ni, Zn and Sn were chosen for substitutional doping in the Cu-phase, since many Cu alloys have these elements in varied compositions [68]. For initial tests, one interfacial Cu atom was replaced by one dopant atom in the Cu/TiN systems and the enthalpy of mixing (ΔH_{mix}) was calculated. Then, ΔH_{mix} for exchanging two interfacial Cu atoms with equal number of dopant atoms, denoted D, were calculated. Such mixing can be expressed in the following form:

$$\text{Cu}_{96}\text{Ti}_{24}\text{N}_{24} + pD^{\text{bulk}} \rightarrow \text{Cu}_{96-p}D_p\text{Ti}_{24}\text{N}_{24} + p\text{Cu}^{\text{bulk}}. \tag{3}$$

where p is the number of dopant atoms exchanged with Cu, and the superscript 'bulk' denotes the energy (per atom) of the most stable crystalline systems for Cu or dopant D. A negative ΔH_{mix} is indicative of energetically favorable mixing. For larger concentrations of dopants (more than two dopant atoms in our system), the number of potential configurations become prohibitively large to identify the minimum energy configurations manually. To remedy this, we adopted a Monte Carlo (MC) randomization technique which we used for doping the Ti/TiN systems in our previous work [41]. To maintain sufficient ergodicity in the process, we ran several sets of such MC searches starting from different initial configurations and checked for convergence to similar energies and configurations.

3. Results and discussion

3.1. Configurations and energies of doped structures

To evaluate the energetic stability of each dopant species at the interface, a single Cu atom was replaced by a dopant atom at the interfacial layers (M = 1 and 2 in Fig. 1(c)) and the ΔH_{mix} was calculated according to Eq. (3). Doping with a Sn atom in the interfacial layers yielded positive enthalpies and the resulting structures were not suitable for interfacial strengthening due to this instability. Hence, Sn was not further considered for interfacial doping. Negative enthalpies ensued from doping with a single atom of Ni or Zn at the M = 1 and 2 layers, implying that substitution with these two species at the interface created stable structures. Next, taking these structures with one dopant atom, another Cu atom from the first two layers was substituted with a dopant of the same species (Ni, for the Ni-doped structure and Zn, for the Zn-doped structure). This resulted in more negative enthalpies as shown in Table 2, where the calculated ΔH_{mix} for each configuration are listed.

To find the low energy structures at higher dopant concentrations, an MC procedure outlined in our previous work was employed [41]. Derived from actual Cu-Zn alloy compositions, we chose two specific concentrations of Zn for doping in to the Cu-phase, which are 5 and 20 mol% [68]. For the system with 96 Cu atoms, exchanging Cu atoms with 5 dopant atoms (Ni or Zn) roughly translate to the dopant concentration

Table 2

ΔH_{mix} for different dopant species. For two dopant atoms, the numbers inside the parentheses indicate the layers, M, at which individual dopant atoms are located.

Dopant Species	Location of Dopants (in layers, M)	ΔH_{mix} (eV/atom)
Ni	(1)	−0.33
	(2)	−0.04
	(1,1)	−0.66
	(1,2)	−0.36
Zn	(1)	−0.30
	(2)	−0.26
	(1,1)	−0.62
	(1,2)	−0.55
Sn	(1)	0.29

of 5 mol%. Similarly, a 20 mol% dopant composition is achieved by replacing 20 Cu atoms with the dopant atoms. Since Cu-Ni is an isomorphous alloy with complete solid solubility between Cu and Ni atoms [69,70], the same concentrations as Zn was chosen for more direct comparisons. Two separate MC runs were initiated for each dopant concentration to test if they converge to similar configurations and energies.

At both compositions studied, the Zn atoms were dispersed throughout the Cu-phase approaching an ideal random solid-solution as shown in Fig. 3(a) and (b). Ni, on the other hand, segregated at the interface for both compositions (5 and 20 mol %). Guided by this MC result, we formed a system with a single layer of Ni at the interface, which amounts to a Ni concentration of 8 mol%. This was done by replacing all the Cu atoms at the interface (eight atoms) with eight Ni atoms, as shown in Fig. 3(c). The ΔH_{mix} for both Zn and Ni at the different compositions are shown in Fig. 3(e). The system with a monolayer of Ni between Cu and TiN gave the lowest energy configuration at the corresponding dopant concentration of 8 mol%. When two Cu layers were replaced with Ni (16 mol%, see Fig. 3(d)), ΔH_{mix} became slightly more negative. Again, this system with two Ni interlayers resulted in the lowest energy configuration at the corresponding dopant compositions (16 mol%), confirming that the Ni segregation at the Cu/TiN interface is favorable. Replacing three or more Cu layers with Ni resulted in ΔH_{mix} becoming slightly less negative, showing that replacing two Cu layers with Ni is the most energetically favorable configuration within the range of dopant concentrations considered. On the other hand, ΔH_{mix} becomes more negative when adding Zn atoms through 20 mol%.

3.2. Ni-Doped configurations

We use the notation $S_{(\text{description})}^{\text{Ni or Zn}}$ to indicate different doped configurations from this point forward. The superscript denotes the dopant species (Ni or Zn) used in the configuration and the subscript gives a unique description of the configuration in terms of dopant location (M, in Fig. 1(c)) or dopant concentration. In case of Ni interlayers inserted at the Cu/TiN interface (as discussed in the previous section), the subscript only mentions the number of layers inserted. For instance, $S_{(\text{bilayer})}^{\text{Ni}}$ implies that the configuration has two layers of Ni inserted at the interface (Fig. 3(d)), $S_{(1,1)}^{\text{Zn}}$ refers to the configuration doped with two Zn atoms both at M = 1 layer and $S_{(5\%)}^{\text{Zn}}$ suggests the configuration with 5 mol % Zn as shown in Fig. 3(a).

3.2.1. Shear resistance

As mentioned earlier, the weakest plane in the undoped systems is at the Cu/TiN interface with TiN (P = 0 in Fig. 1(c)). To evaluate whether Ni doping strengthens the shear resistance of this plane, GSFE calculations described in Sec. 2.2. were carried out at the interface with TiN. Fig. 4(a) shows the GSFE plots along $\text{X}\|\left[11\bar{2}\right]_{\text{Cu}}$ for some of the Ni-
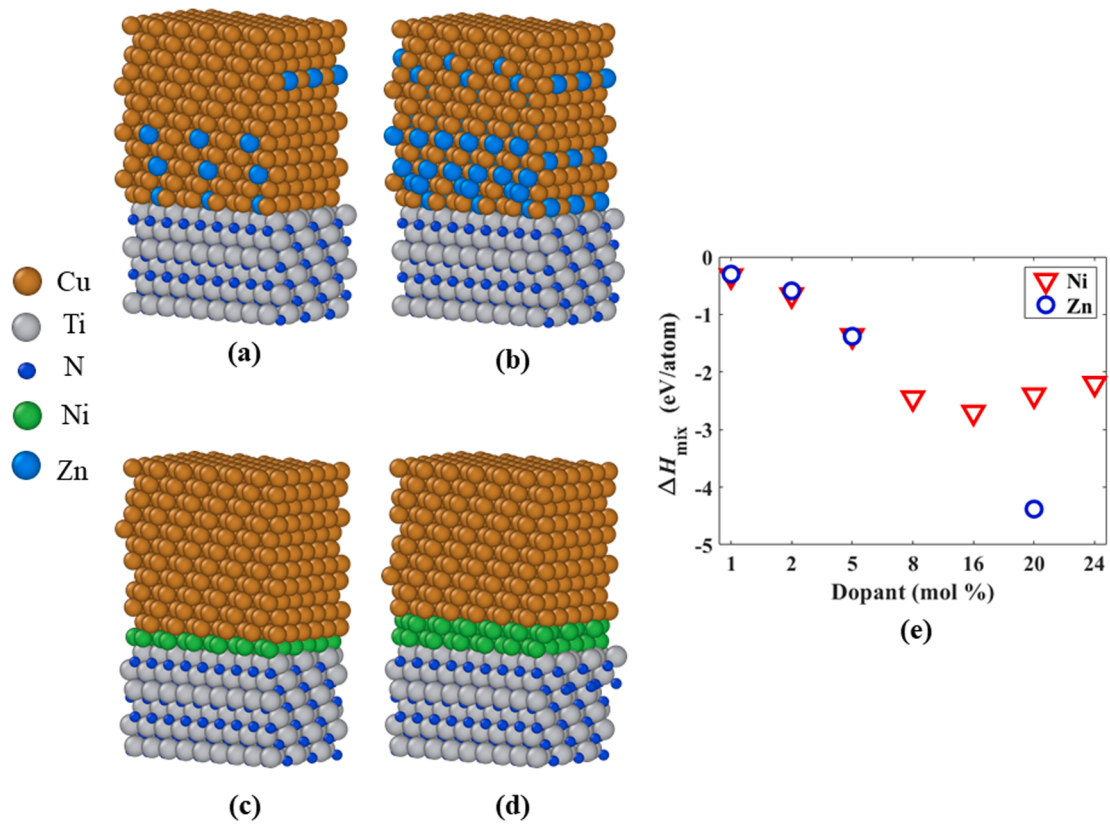
Fig. 3. Snapshots of Cu/TiN doped with Zn at (a) 5 mol% and (b) 20 mol%. (c) Cu/Ni$_{(Monolayer)}$/TiN and (d) Cu/Ni$_{(Bilayer)}$/TiN systems. (e) Enthalpy of mixing for different dopant concentrations of both species.
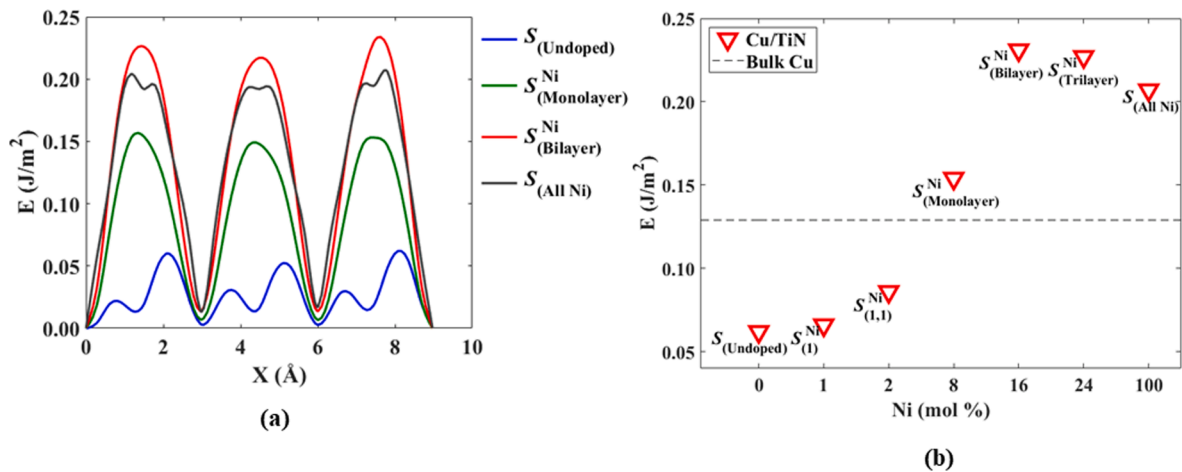

Fig. 4. (a) GSFE along X$\|\left[11\overline{2}\right]_{Cu}$ along for P = 0 of Cu/TiN systems doped with Ni at different compositions. (b) Maximum barrier height as a function of mol% of Ni.

doped systems compared to the undoped system, $S_{(undoped)}$. The GSFE plots are characterized by three local minima along X, and the global minimum only repeats after sampling the whole length of the simulation box in X. The highest peak from these GSFE plots represent the energy barrier for shear displacement. Such barrier heights were extracted from GSFE plots of all the Ni-doped systems discussed in Sec. 3.1. and are plotted as functions of dopant concentration in Fig. 4(b). In comparison to the undoped system, the barrier heights increase slightly in configurations that have one and two Ni atoms at the interfacial layer M = 1, represented as $S_{(1)}^{Ni}$ and $S_{(1,1)}^{Ni}$, respectively. With a monolayer of Ni between Cu and TiN, the P = 0 plane, which is now the interface between

Ni and TiN, has a significantly higher barrier height, such that it surpasses the barrier height between two Cu layers in bulk Cu. The bulk Cu barrier is shown with dotted lines in Fig. 4(b). A Ni bilayer inserted between Cu and TiN exhibits the highest barrier height at P = 0, while more interlayers reduce the barrier from this maximum.

In the comparison of barrier heights shown in Fig. 4(b), only the barrier heights at the interfaces with TiN (P = 0) were considered. However, the introduction of Ni interlayers between Cu and TiN creates another hetero interface which is between Cu and Ni. For the $S_{(Bilayer)}$ configuration, this Cu/Ni interface occurs at P = 2 plane as shown in Fig. 5(a). We tested the barrier heights of P = 0–4 planes for the $S_{(bilayer)}^{Ni}$
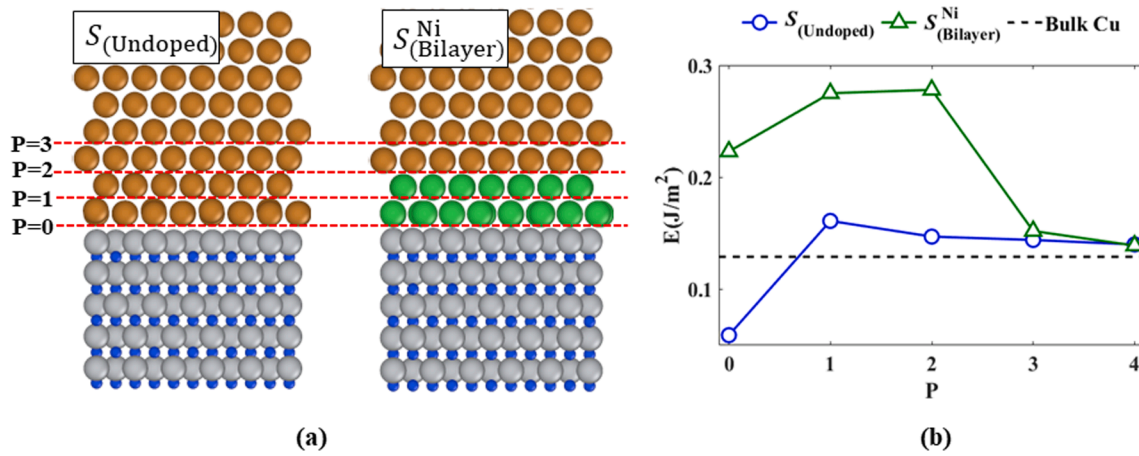
Fig. 5. (a) Interfacial planes marked with P for $S_{(Undoped)}$ and $S_{(Bilayer)}^{Ni}$ configurations, and (b) barrier heights at these interfacial planes in comparison with the bulk Cu.

configuration and compared the results with undoped system in Fig. 5 (b). Evidently, the interfacial planes P = 0–2 have much higher barrier in $S_{(bilayer)}^{Ni}$ compared to the undoped system. Within the $S_{(bilayer)}^{Ni}$ system, the planes in contact with Ni have much higher GSFE barriers than bulk Cu. Only after being one or more layers away from the Ni layers (P = 3 and 4) does the GSFE barrier approach bulk Cu. Furthermore, it can be observed that the lowest GSFE barrier, by far, is at the Cu/TiN interface (P = 0) for the undoped system, and sandwiching Ni in between these interfaces results in an *order of magnitude* increase in the lowest interfacial GSFE barrier.

3.2.2. Tensile strength

As outlined in Sec. 2.3, the stress-strain relations under uniaxial tensile loading were evaluated for the systems doped with Ni. In Fig. 6 (a), stress vs. strain plots for three Ni-doped configurations are compared with the undoped systems until fracture occurs. There is an increase in both the stress as a function of strain, and the extent of strain before fracture when Ni doping is present. For the $S_{(All Ni)}$ case, there is a very large increase in stress as a function strain, which is likely due to the fact that Ni has a much higher elastic modulus than Cu [71]. As shown in Fig. 6(b)-(e), Ni-doped systems mostly break-off between the first and second Cu layers under tensile loading. For instance, in the undoped system shown in Fig. 6(b), this break-off plane is at P = 1
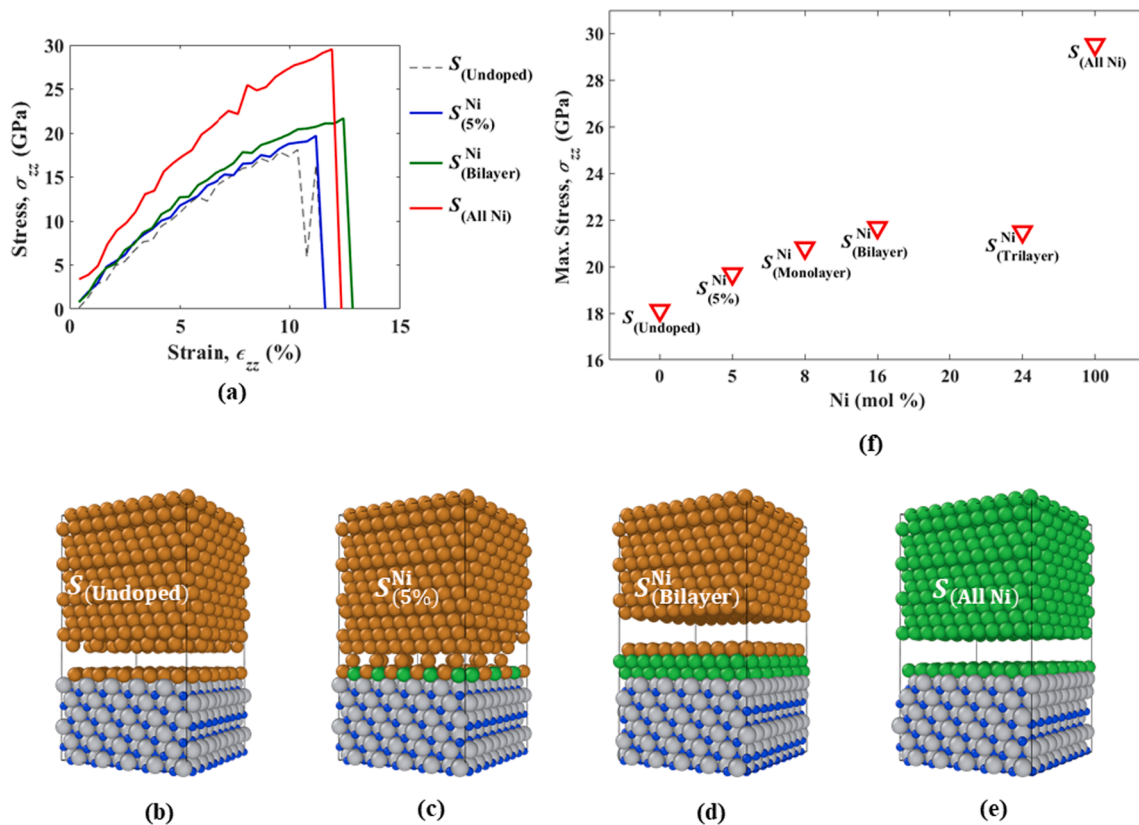

Fig. 6. (a) Stress vs. strain plot and (b-e) snapshots immediately after fracture for four configurations (one undoped and three Ni-doped). (f) Maximum strength at different Ni compositions.

whereas for the $S_{(\text{bilayer})}^{\text{Ni}}$ system in Fig. 6(d), it is P = 3. The maximum stress before fracture as a function of Ni content is given in Fig. 6(f). Consistent with the stress vs. strain plots, the $S_{(\text{Bilayer})}^{\text{Ni}}$ has the highest tensile strength among the Ni-doped systems, while the $S_{(\text{All Ni})}$ system has the highest tensile strength of all the systems studied. From the results above, the $S_{(\text{Bilayer})}^{\text{Ni}}$ system offers the best option for overall strengthening of the interface among the Cu/TiN systems doped with Ni, with the highest GSFE barrier along with the highest tensile strength.

As stated, both $S_{(\text{Undoped})}$ and $S_{(\text{Bilayer})}^{\text{Ni}}$ fractured at the plane between the first two Cu layers under tensile loading, which is at P = 1 for $S_{(\text{Undoped})}$ and P = 3 for $S_{(\text{Bilayer})}^{\text{Ni}}$ (see Fig. 6). To better understand the energetics of this, the WoA is compared between the $S_{(\text{Undoped})}$ and $S_{(\text{Bilayer})}^{\text{Ni}}$ systems in Fig. 7. Consistent with where tensile failure occurs, the WoA is weakest at P = 1 for $S_{(\text{Undoped})}$. For $S_{(\text{Bilayer})}^{\text{Ni}}$, since the WoA in the P = 3 layer is slightly larger than for P > 3, it shows that WoA isn't an exact descriptor for where tensile fracture occurs. For this system, the best indicator of where tensile fracture occurs is where the WoA has a large reduction that approaches the minimum WoA.

3.2.3. Electronic analysis

To understand the strengthening mechanism of the Ni interlayers, we examined the electron density of the systems provided by DFT calculations. For metal-metal bonds, the minimum electron density in between them can provide a qualitative estimate of the bonding strength with higher magnitude implying stronger binding and resistance to shear [28]. The average electron density for the Cu/TiN systems, $\rho(z)$, was calculated as a function of position in the $Z\|[111]_{\text{Cu}}\|[111]_{\text{TiN}}$ direction. This plane-averaged electron density, $\rho(z)$, was then scaled by $(\rho_{\text{bulk}}^{\min})$, the minima of the plane-averaged electron density calculated similarly along $Z\|[111]_{\text{Cu}}$ for bulk Cu. Fig. 8(a) gives a comparison of this normalized electron density $\rho(z)/\rho_{\text{bulk}}^{\min}$, as a function of Z position for the $S_{(\text{Undoped})}$ and $S_{(\text{Bilayer})}^{\text{Ni}}$ systems, along with snapshots of the systems showing electron density isosurfaces. The location of the P = 1, 2 and 3 planes in the plot are marked by red dotted lines, which are vertically extended and aligned to the corresponding planes in the snapshots below. The normalized densities in Fig. 8(a) have a few subtle features that are important in our analysis: (a) the TiN electron density appears to be unaffected by the presence or absence of the interfacial Ni bilayer, (b) the extra electron in Cu $[3d^{10}4s^1]$ compared to Ni $[3d^84s^2]$ is reflected in the larger electron density peaks for the undoped system, (c) the minima in $\rho(z)/\rho_{\text{bulk}}^{\min}$ are deeper at P = 0 and 1 in the undoped system compared to the doped one, and (d) the Ti-Ni distance at the interface is smaller in the bilayer system than the Ti-Cu distance in the undoped system. The

Fig. 7. Work of adhesion at interfacial planes for $S_{(\text{Undoped})}$ and $S_{(\text{Bilayer})}^{\text{Ni}}$.

shallower density minima at P = 0 and P = 1 for the Ni bilayer system suggests that the presence of the Ni increases the electron density at the interface, leading to the increased shear resistance in between metal layers due to their "glue-like" behavior [28].

The increase in interfacial electron density is more readily apparent in Fig. 8(b), which compares the electron density minima as a function of layer for the $S_{(\text{Undoped})}$ and $S_{(\text{Bilayer})}^{\text{Ni}}$ systems. For the undoped system, the electron density is the lowest at the interface P = 0, where the GSFE barrier height is the smallest, and steadily increases with P until it approaches that of bulk Cu. In contrast, the $S_{(\text{Bilayer})}^{\text{Ni}}$ electron densities at P = 0–2, where Ni atoms are present, are significantly higher than in bulk Cu. For P = 3–4, the electron densities are very similar to that for bulk Cu. Overall, there is a correlation between the barrier heights of the interfacial planes (P = 0–4) plotted in Fig. 5(b) and the electron density for the same planes in Fig. 8(b). This suggests that Ni interlayers increase the resistance to shear at Cu/TiN interfacial region by increasing the electron density between the (1 1 1) atomic layers in this region.

The increased interfacial electron density with Ni bilayers may be due to differences in electron transfer between the interfacial layers of the $S_{(\text{Undoped})}$ and $S_{(\text{Bilayer})}^{\text{Ni}}$ systems. To better understand this, the partial density of states (PDOS) of the *unoccupied s and d*-orbitals (i.e., states above the Fermi level E_F) for all interfacial Ni and Cu atoms were calculated along with their values when the same number of Ni or Cu atoms are in their respective intrinsic bulk systems. The PDOS was calculated by sampling the energy band in ~3 meV intervals and using the tetrahedron method with Blöchl corrections [72] for smearing with $6 \times 12 \times 2$ k-points. The PDOS are given in Fig. S1 in the supplementary information. To compare interfacial Cu and Ni PDOS for *s* and *d*-orbitals with their intrinsic bulk values, the difference between the total number of unoccupied orbitals of a particular type (4*s* or 3*d*) of interfacial Cu and Ni atoms with their respective bulk values, $\Delta_{\text{Unocc.}}\text{T} = \text{T}_{\text{Interface}}^{\text{Unocc.}} - \text{T}_{\text{Bulk}}^{\text{Unocc.}}$, are given in Table 3. These totals are proportional to the area under the PDOS curves shown in Fig. S1. Negative values denote a decrease in the number of unoccupied states—as a result of electron occupation—for a specific orbital. In other words, the more negative a value, the fewer are the unoccupied states that remain when the atoms are brought in contact with TiN.

These results show that contact with TiN decreases the number of unoccupied states in both Cu and Ni, but the effect is more significant in the case of Ni. Considerations of atomic electronic configurations are useful in understanding this result. Interfacial Cu atoms have both their 4*s* and 3*d* orbitals filled to a similar degree in comparison with bulk. Ni, though, has a factor of ten increase in the number of filled 3*d* orbitals in comparison to 4*s*. Moreover, the total number of states filled is significantly higher for Ni than Cu, in comparison with their respective bulk values. The ground state electron configuration for the valence electrons of Cu is $4s^13d^{10}$ [73], which primarily provides an unoccupied 4*s* orbital to accept an electron from interfacial Ti. On the other hand, Ni has a configuration of $4s^23d^8$, which provides two 3*d* states to be filled. The increase in occupancy of the 3*d* orbitals for Ni should have two consequences that increase binding with Ti. The first is having more available electrons for bonding, which is consistent with the electron density results in Fig. 8. Second, the bonding will have more 3*d* orbital character for Ni, which is more compact than the 4*s* orbital that is more prevalent for Cu. This is consistent with the observation made above in the context of Fig. 8(a)—that the Ti-Ni distance at the interface is smaller in the bilayer system than the Ti-Cu distance in the undoped system—and is reflected in the average distance between interfacial Ni and Ti atoms of 2.08 Å, compared to the average distance between interfacial Cu and Ti atoms of 2.24 Å.

3.3. Zn-doped configurations

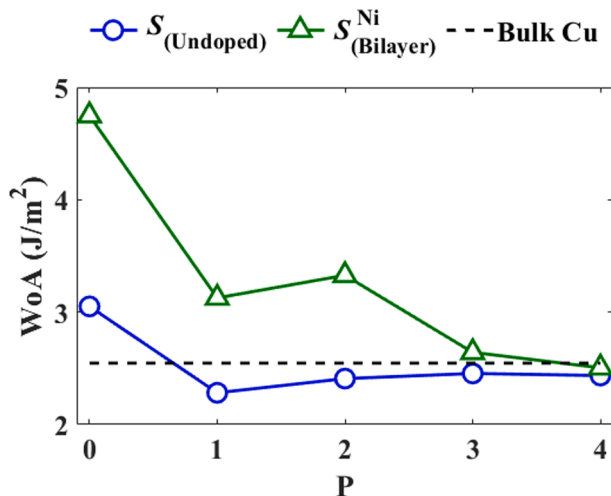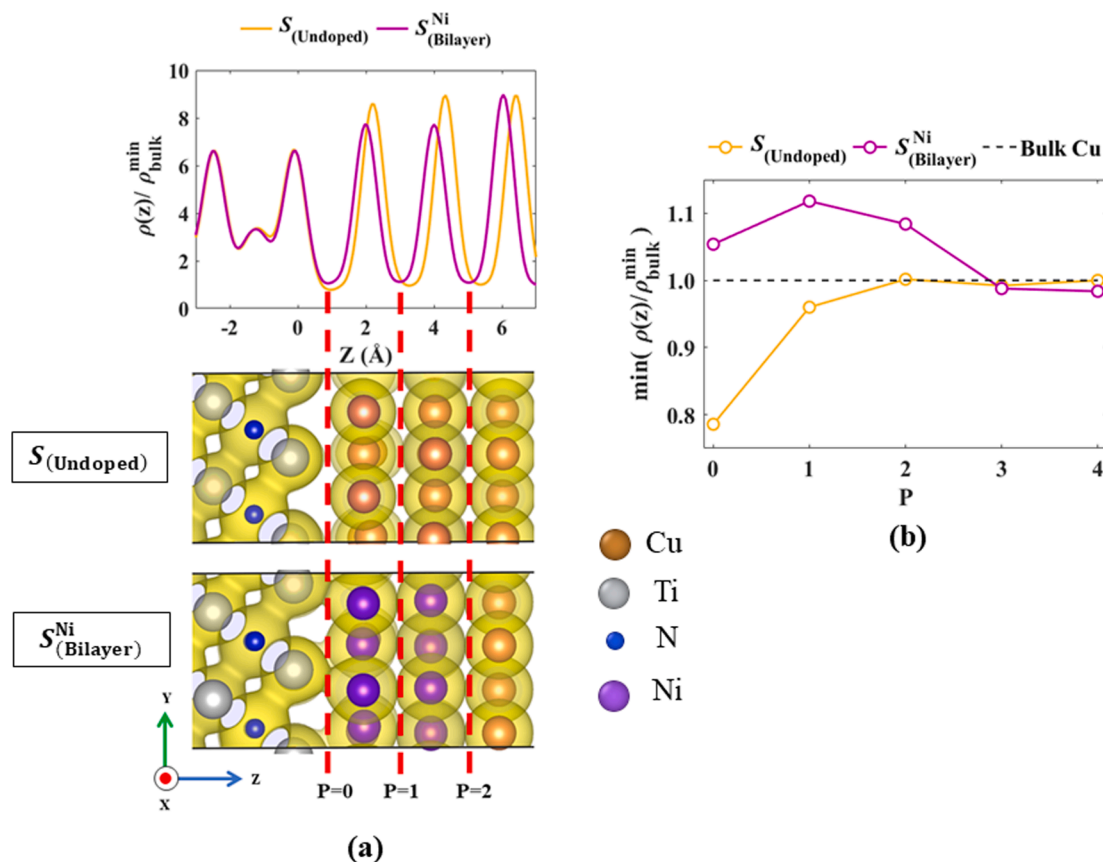For Zn-doped configurations, the GSFE at the weakest layer (P = 0)

Fig. 8. (a) Plane-averaged electron density as a function of z positions in $S_{(Undoped)}$ and $S_{(Bilayer)}^{Ni}$ along with the snapshots of the electron density isosurfaces. (b) Average electron density in the planes (P) between the metal layers.

Table 3
Difference in the total number of unoccupied orbitals of a given type (see text) of interfacial atoms from their respective bulk atoms.

Interfacial Atoms Systems	Cu $S_{(Undoped)}$		Ni $S_{(Bilayer)}^{Ni}$	
Orbital	$3d$	$4s$	$3d$	$4s$
$\Delta_{Unocc.}$ T	−822.7	−515.1	−1961.4	−224.1

were calculated and plotted against $X \parallel [11\bar{2}]_{Cu}$ as was done for the Ni-doped systems. The detailed GSFE plots are shown in the supplementary Fig. S2. Barrier heights obtained from the GSFE curves are plotted as a function of Zn dopant concentration in Fig. 9(a). As can be observed, there is a direct correlation between barrier height and Zn concentration. At 5 mol % concentration and higher, the barrier height exceeds that of bulk Cu. Within the range of Zn-doped systems studied, the highest barrier is 0.218 J/m^2 at 20 mol % Zn, which is close to the barrier height for the Ni-doped configuration at a similar dopant composition (0.227 J/m^2). The stress vs. strain plots for the Zn-doped configurations are shown in Fig. S3 in the supplementary information. Fig. 9(b) gives the tensile strength as a function of Zn-doping. In contrast to what is observed for GSFE barriers, the tensile strength inversely correlates with Zn concentration. Both Zn-doped systems broke off at P = 1 as occurred for the undoped system. In summary, Zn-doping increases the GSFE barriers, but decreases tensile strength.

To understand the role of Zn in increasing the GSFE barriers, the following analysis can be used. Highly electronegative nitrogen atoms (3.04 on the Pauling scale) induce net positive charges on the interfacial Ti atoms in TiN. Interfacial Cu atoms next to the Ti atoms carry small

negative charges due to the difference between the electronegativities of Ti and Cu (1.54 vs. 1.90, respectively) [74]. This is confirmed by analysis of layer-averaged Bader charges [75,76] in Fig. 9(c), which shows that the interfacial Ti layer (denoted by M = −1) has a net positive charge of 1.32e/atom, whereas the Cu layer (M = 1) next to Ti carries a net negative charge of −0.28e/atom. Zn has a lower electronegativity (1.65) than Cu (1.90) [74], which results in Zn having a more positive charge.

Due to electrostatics, the more positively charged Zn atoms will have weaker interactions with interfacial Ti atoms than Cu. This weakens the overall interactions with interfacial Ti with Zn-doped Cu than undoped Cu, which should decrease their tensile strength. On the other hand, the GSFE barriers increase with Zn doping. Evaluating the GSFE plot (Fig. 2 (b)), the minimum energy configuration will have Zn in the "hole" position, where its location is relatively far away from neighboring Cu atoms (see Fig. 9(d)). At the GSFE barrier (see Fig. 9(e)), the Zn atom approaches an interfacial Ti atom, where its positive charge will have a greater effect on the interaction than in the hole position. As a consequence, while the minimum energy configuration of Zn-doped Cu has weaker interactions with TiN than undoped Cu, the GSFE barrier configuration will have an even greater impact from Zn doping due to the proximity of Zn to interfacial Ti. This leads to a greater difference in energy between the two configurations, leading to a larger GSFE barrier.

4. Conclusion

First principles DFT was used to study the impact of doping Cu/TiN metal/ceramic interfaces with Ni, Zn and Sn. Guided by enthalpies of mixing and aided by a MC procedure, it was found that substitutional doping of interfacial Cu atoms with Ni and Zn created stable structures, while this was not the case for Sn. Ni segregated at the interface forming interlayers between Cu and TiN, while Zn dispersed throughout the
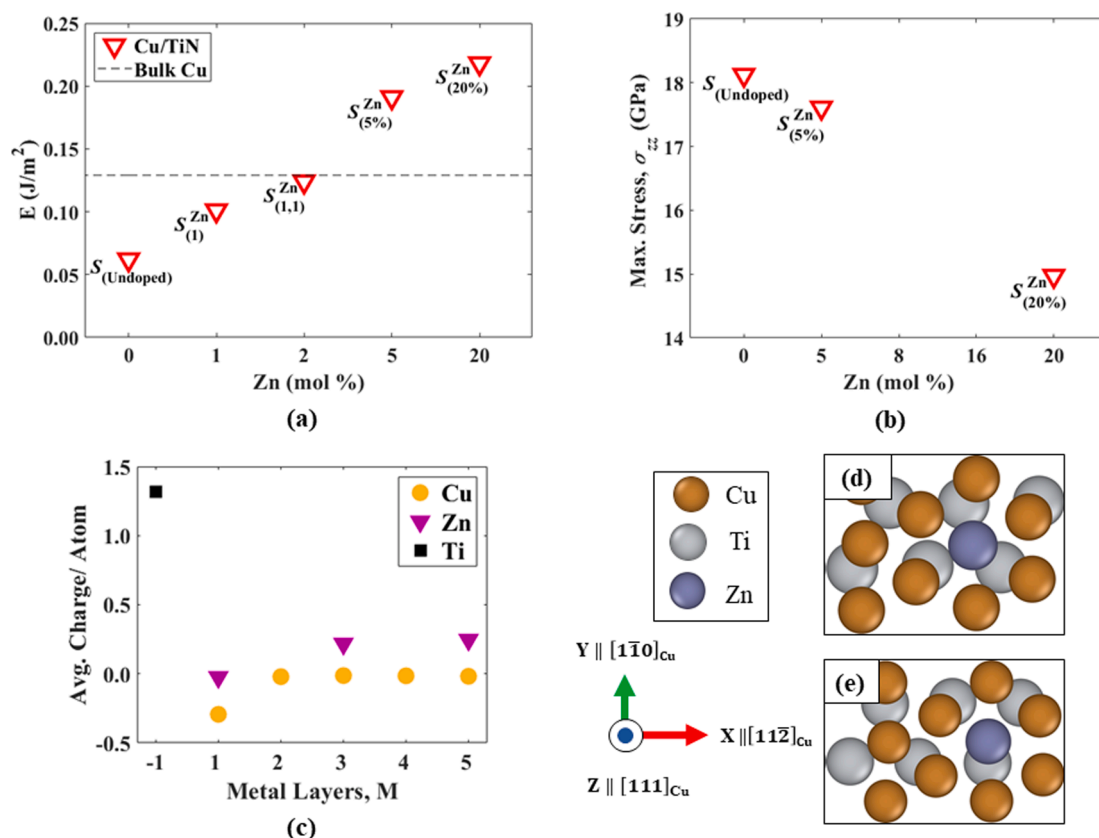
Fig. 9. (a) Barrier height and (b) maximum strength at different Zn compositions. (c) Average Bader charge per atom for each metal layer in the system with 5 mol% Zn. Snapshots of the interfacial Cu and Ti layers viewed from Z-direction, corresponding to the (d) minimum and (e) maximum energy configurations in the GSFE plot for 5 mol% Zn-doped system.

system yielding a solid solution. Energy barriers to shear displacement and maximum tensile strength were calculated in each case as measures of the interfacial strength. Incorporating Ni interlayers at the interface significantly increases both, while Zn-doping improved the resistance to shear but decreased the tensile strength.

Among the Ni-doped configurations, an interlayer consisting of two atomic layers of Ni inserted between the Cu and TiN was the most stable. This configuration also had the highest barrier to shear at the interface and the largest tensile strength. Acting as 'electron glue' at the interface, these Ni atomic layers increased the interfacial electron density and reduced the interplanar distance, raising the barrier to shear much higher than the undoped system. The enhancement in electron density is linked to the availability of two $3d$ states in Ni compared to one $4s$ state in Cu, which allows more electrons to bond with Ni. Moreover, this Ni bonding of predominantly $3d$-orbital character is radially more compact than the $4s$-orbital bonding in Cu, reducing the interfacial distance with Ti. Although shear strength increases with Zn-doping, the tensile strength decreases significantly. This was linked to weaker interactions between Zn and Ti atoms. The weaker Zn/Ti interaction caused weaker binding overall at Zn-doped Cu/TiN interfaces. However, at the GSFE barrier, Zn atoms came in closer contact with Ti than in the minimum energy configuration, creating a larger difference in energy between GSFE barrier and minimum energies, causing the overall GSFE barrier to increase. Our results indicate that sub-nm Ni interlayers deposited between Cu and TiN may enhance the overall mechanical integrity of the Cu/TiN interface, a conclusion remaining to be tested through experimentation.

Declaration of Competing Interest

The authors declare that they have no known competing financial interests or personal relationships that could have appeared to influence the work reported in this paper.

Appendix A. Supplementary material

Supplementary data to this article can be found online at https://doi.org/10.1016/j.apsusc.2021.149562.

References

[1] B. Cantor, F. Dunne, I. Stone, Institute of Physics (Great Britain), Oxford-Kobe Materials Seminar (3rd : 2000 : Kobe Institute), Metal and ceramic matrix composites: an Oxford-Kobe materials text, 2004, 429.

[2] N. Chawla, K.K. Chawla, Metal matrix composites, 2013. https://doi.org/10.1007/978-1-4614-9548-2.

[3] J.S. Moya, S. Lopez-Esteban, C. Pecharromán, The challenge of ceramic/metal microcomposites and nanocomposites, Prog. Mater. Sci. 52 (2007) 1017–1090, https://doi.org/10.1016/j.pmatsci.2006.09.003.

[4] J. Horník, S. Krum, D. Tondl, M. Puchnin, P. Sachr, L. Cvrček, Multilayer coatings Ti/TiN, Cr/CrN AND W/WN deposited by magnetron sputtering for improvement of adhesion to base materials, Acta Polytech. 55 (2015) 388–392, https://doi.org/10.14311/AP.2015.55.0388.

[5] F.-Y. Lin, A. Chernatynskiy, J.C. Nino, J.L. Jones, R. Hennig, S.B. Sinnott, Role of composition and structure on the properties of metal/multifunctional ceramic interfaces, J. Appl. Phys. 120 (2016), 045310, https://doi.org/10.1063/1.4959074.

[6] R. Polanco, A. De Pablos, P. Miranzo, M.I. Osendi, Metal–ceramic interfaces: joining silicon nitride–stainless steel, Appl. Surf. Sci. 238 (2004) 506–512, https://doi.org/10.1016/j.apsusc.2004.05.290.

[7] M. Halbig, M. Jaskowiak, J. Kiser, D. Zhu, Evaluation of ceramic matrix composite technology for aircraft turbine engine applications, in: 51st AIAA Aerosp. Sci. Meet. Incl. New Horizons Forum Aerosp. Expo., American Institute of Aeronautics and Astronautics, Reston, Virgina, 2013. https://doi.org/10.2514/6.2013-539.

[8] J.C. Jiang, W.J. Meng, A.G. Evans, C.V. Cooper, Structure and mechanics of W-DLC coated spur gears, Surf. Coatings Technol. 176 (2003) 50–56, https://doi.org/10.1016/S0257-8972(03)00445-6.

[9] M.N. Kotzalas, G.L. Doll, Tribological advancements for reliable wind turbine performance, Philos. Trans. R. Soc. A Math. Phys. Eng. Sci. 368 (2010) 4829–4850, https://doi.org/10.1098/rsta.2010.0194.

[10] D. Ham, J. Lee, Transition metal carbides and nitrides as electrode materials for low temperature fuel cells, Energies. 2 (2009) 873–899, https://doi.org/10.3390/en20400873.

[11] A. Vereschaka, E. Kataeva, N. Sitnikov, A. Aksenenko, G. Oganyan, C. Sotova, Influence of thickness of multilayered nano-structured coatings Ti-TiN-(TiCrAl)N and Zr-ZrN-(ZrCrNbAl)N on tool life of metal cutting tools at various cutting speeds, Coatings. 8 (2018) 44, https://doi.org/10.3390/coatings8010044.

[12] J. Carmai, F. Dunne, Chapter 11 Manufacture of ceramic fibre metal matrix composites, in: Met. Ceram. Matrix Compos., 2004.

[13] F. Dunne, B. Cantor, I. Stone, eds., Metal and Ceramic Matrix Composites, Taylor & Francis, 2003. https://doi.org/10.1201/9781420033977.

[14] K.U. Kainer, ed., Metal Matrix Composites, Wiley-VCH Verlag GmbH & Co. KGaA, Weinheim, FRG, 2006. https://doi.org/10.1002/3527608117.

[15] K. Holmberg, A. Matthews, Coatings Tribology: Properties, Mechanisms, Techniques and Applications in Surface Engineering, Elsevier, 2009.

[16] N. Li, X.Y. Liu, Review: mechanical behavior of metal/ceramic interfaces in nanolayered composites—experiments and modeling, J. Mater. Sci. (2017) 1–22, https://doi.org/10.1007/s10853-017-1767-1.

[17] S. Shao, A. Misra, H. Huang, J. Wang, Micro-scale modeling of interface-dominated mechanical behavior, J. Mater. Sci. 53 (2018) 5546–5561, https://doi.org/10.1007/s10853-017-1662-9.

[18] S. Pathak, N. Li, X. Maeder, R.G. Hoagland, J.K. Baldwin, J. Michler, A. Misra, J. Wang, N.A. Mara, On the origins of hardness of Cu–TiN nanolayered composites, Scr. Mater. 109 (2015) 48–51, https://doi.org/10.1016/j.scriptamat.2015.07.015.

[19] D.H.R. Fors, G. Wahnström, Theoretical study of interface structure and energetics in semicoherent Fe(001)/MX(001) systems (M=Sc, Ti, V, Cr, Zr, Nb, Hf, Ta; X=C or N), Phys. Rev. B - Condens. Matter Mater. Phys. 82 (2010) 1–13. https://doi.org/10.1103/PhysRevB.82.195410.

[20] G. Pilania, B.J. Thijsse, R.G. Hoagland, I. LaziÄ, S.M. Valone, X.Y. Liu, Revisiting the Al/Al 2 O 3 interface: Coherent interfaces and misfit accommodation, Sci. Rep. 4 (2014) 1–9, https://doi.org/10.1038/srep04485.

[21] I. Salehinia, S. Shao, J. Wang, H.M. Zbib, Interface structure and the inception of plasticity in Nb/NbC nanolayered composites, Acta Mater. 86 (2015) 331–340, https://doi.org/10.1016/j.actamat.2014.12.026.

[22] T. Liang, M. Ashton, K. Choudhary, D. Zhang, A.F. Fonseca, B.C. Revard, R. G. Hennig, S.R. Phillpot, S.B. Sinnott, Properties of Ti/TiC interfaces from molecular dynamics simulations, J. Phys. Chem. C 120 (2016) 12530–12538, https://doi.org/10.1021/acs.jpcc.6b02763.

[23] L. Rao, H. Liu, S. Liu, Z. Shi, X. Ren, Y. Zhou, Q. Yang, Interface relationship between TiN and Ti substrate by first-principles calculation, Comput. Mater. Sci. 155 (2018) 36–47, https://doi.org/10.1016/j.commatsci.2018.08.028.

[24] V. Bonu, M. Jeevitha, V. Praveen Kumar, H.C. Barshilia, Nanolayered multilayer Ti/TiN coatings: Role of bi-layer thickness and annealing on solid particle erosion behaviour at elevated temperature, Surf. Coatings Technol. 357 (2019) 204–211, https://doi.org/10.1016/j.surfcoat.2018.10.007.

[25] W. Yang, G. Ayoub, I. Salehinia, B. Mansoor, H. Zbib, The effect of layer thickness ratio on the plastic deformation mechanisms of nanoindented Ti/TiN nanolayered composite, Comput. Mater. Sci. 154 (2018) 488–498, https://doi.org/10.1016/j.commatsci.2018.08.021.

[26] T. Sun, X. Wu, R. Wang, W. Li, Q. Liu, First-principles study on the adhesive properties of Al/TiC interfaces: Revisited, Comput. Mater. Sci. 126 (2017) 108–120, https://doi.org/10.1016/j.commatsci.2016.09.024.

[27] X. Zhang, S. Shao, A.S.M. Miraz, C.D. Wick, B.R. Ramachandran, W.J. Meng, Low temperature growth of Cu thin films on TiN(001) templates: Structure and energetics, Materialia. 12 (2020) 100748, https://doi.org/10.1016/j.mtla.2020.100748.

[28] A.S. Mohammad Miraz, S. Sun, S. Shao, W.J. Meng, B.R. Ramachandran, C. D. Wick, Computational study of metal/ceramic interfacial adhesion and barriers to shear displacement, Comput. Mater. Sci. 168 (2019) 104–115, https://doi.org/10.1016/j.commatsci.2019.06.006.

[29] J. Qin, Q. Huang, X. Wang, X. Suo, J. Wang, H. Li, Interfacial metal/ceramic bonding mechanism for metallization of ceramics via cold spraying, J. Mater. Process. Technol. 288 (2021) 116845, https://doi.org/10.1016/j.jmatprotec.2020.116845.

[30] R. Goswami, S.B. Qadri, N. Bernstein, A. Moser, Role of microstructure and interfaces in governing the mechanical properties of nanocomposites manufactured in the solid state, JOM. 72 (2020) 2875–2881, https://doi.org/10.1007/s11837-020-04138-z.

[31] J. Huang, S. Daryadel, M. Minary-Jolandan, Low-cost manufacturing of metal-ceramic composites through electrodeposition of metal into ceramic scaffold, ACS Appl. Mater. Interfaces. 11 (2019) 4364–4372, https://doi.org/10.1021/acsami.8b18730.

[32] Q. Li, P. Song, X. He, X. Yu, C. Li, T. Huang, K. Lü, Y. Zhou, J. Lu, Plastic metallic-barrier layer for crack propagation within plasma-sprayed Cu/ceramic coatings, Surf. Coatings Technol. 360 (2019) 259–268, https://doi.org/10.1016/j.surfcoat.2018.12.124.

[33] L. Chen, J. Paulitsch, Y. Du, P.H. Mayrhofer, Thermal stability and oxidation resistance of Ti-Al-N coatings, Surf. Coatings Technol. 206 (2012) 2954–2960, https://doi.org/10.1016/j.surfcoat.2011.12.028.

[34] S.C. PalDey, S.C. Deevi, Single layer and multilayer wear resistant coatings of (Ti, Al)N: A review, Mater. Sci. Eng. A. 342 (2003) 58–79, https://doi.org/10.1016/S0921-5093(02)00259-9.

[35] A.S. Bochkarev, M.N. Popov, V.I. Razumovskiy, J. Spitaler, P. Puschnig, Ab initio study of Cu impurity diffusion in bulk TiN, Phys. Rev. B. 94 (2016), 104303, https://doi.org/10.1103/PhysRevB.94.104303.

[36] W. Tillmann, E. Vogli, S. Momeni, Mechanical and tribological properties of Ti/TiAlN duplex coatings on high and low alloy tool steels, Vacuum 84 (2009) 387–392, https://doi.org/10.1016/j.vacuum.2009.08.001.

[37] E. Vogli, W. Tillmann, U. Selvadurai-Lassl, G. Fischer, J. Herper, Influence of Ti/TiAlN-multilayer designs on their residual stresses and mechanical properties, Appl. Surf. Sci. 257 (2011) 8550–8557, https://doi.org/10.1016/j.apsusc.2011.05.013.

[38] J.M. Lackner, L. Major, M. Kot, Microscale interpretation of tribological phenomena in Ti/TiN soft-hard multilayer coatings on soft austenite steel substrates, Bull. Polish Acad. Sci. Tech. Sci. 59 (2011) 343–356, https://doi.org/10.2478/v10175-011-0042-x.

[39] D.B. Miracle, O.N. Senkov, A critical review of high entropy alloys and related concepts, Acta Mater. 122 (2017) 448–511, https://doi.org/10.1016/j.actamat.2016.08.081.

[40] Z. Li, S. Zhao, R.O. Ritchie, M.A. Meyers, Mechanical properties of high-entropy alloys with emphasis on face-centered cubic alloys, Prog. Mater. Sci. 102 (2019) 296–345, https://doi.org/10.1016/j.pmatsci.2018.12.003.

[41] A.S.M. Miraz, E. Williams, W.J. Meng, B.R. Ramachandran, C.D. Wick, Improvement of Ti/TiN interfacial shear strength by doping – A first principles density functional theory study, Appl. Surf. Sci. 517 (2020), 146185, https://doi.org/10.1016/j.apsusc.2020.146185.

[42] L. Ipaz, J.C. Caicedo, J. Esteve, F.J. Espinoza-Beltran, G. Zambrano, Improvement of mechanical and tribological properties in steel surfaces by using titanium–aluminum/titanium–aluminum nitride multilayered system, Appl. Surf. Sci. 258 (2012) 3805–3814, https://doi.org/10.1016/j.apsusc.2011.12.033.

[43] D.A. Colombo, A.D. Mandri, M.D. Echeverría, J.M. Massone, R.C. Dommarco, Mechanical and tribological behavior of Ti/TiN and TiAl/TiAlN coated austempered ductile iron, Thin Solid Films 647 (2018) 19–25, https://doi.org/10.1016/j.tsf.2017.12.014.

[44] G. Feldbauer, M. Wolloch, P.O. Bedolla, J. Redinger, A. Vernes, P. Mohn, Suppression of material transfer at contacting surfaces: The effect of adsorbates on Al/TiN and Cu/diamond interfaces from first-principles calculations, J. Phys. Condens. Matter. 30 (2018), https://doi.org/10.1088/1361-648X/aaac91.

[45] T. Sun, X. Wu, W. Li, R. Wang, The mechanical and electronic properties of Al/TiC interfaces alloyed by Mg, Zn, Cu, Fe and Ti: First-principles study, Phys. Scr. 90 (2015), https://doi.org/10.1088/0031-8949/90/3/035701.

[46] H.Z. Zhang, S.Q. Wang, The effects of Zn and Mg on the mechanical properties of the Al/TiN interface: A first-principles study, J. Phys. Condens. Matter. 19 (2007), https://doi.org/10.1088/0953-8984/19/22/226003.

[47] Z.G. Liu, C.Y. Wang, T. Yu, Influence of Re on the propagation of a Ni/Ni3Al interface crack by molecular dynamics simulation, Model. Simul. Mater. Sci. Eng. 21 (2013), https://doi.org/10.1088/0965-0393/21/4/045009.

[48] Y.X. Wu, Y.Y. Li, Y.M. Wang, First-principles study of the influence of lattice misfit on the segregation behaviors of hydrogen and boron in the Ni-Ni3Al system, Acta Mater. 55 (2007) 4845–4852, https://doi.org/10.1016/j.actamat.2007.05.006.

[49] L. Peng, P. Peng, D.D. Wen, Y.G. Liu, H. Wei, X.F. Sun, Z.Q. Hu, Site preference of S-doping and its influence on the properties of a Ni/Ni3Al interface, Model. Simul. Mater. Sci. Eng. 19 (2011), https://doi.org/10.1088/0965-0393/19/6/065002.

[50] G. Elssner, D. Korn, M. Rühle, The influence of interface impurities on fracture energy of UHV diffusion bonded metal-ceramic bicrystals, Scr. Metall. Mater. 31 (1994) 1037–1042, https://doi.org/10.1016/0956-716X(94)90523-1.

[51] H. Nahor, Y. Kauffmann, W.D. Kaplan, The Cr-Doped Ni-YSZ(111) interface: Segregation, oxidation and the Ni equilibrium crystal shape, Acta Mater. 166 (2019) 28–36, https://doi.org/10.1016/j.actamat.2018.12.023.

[52] T.X. Liang, Y.Q. Liu, Z.Q. Fu, T.Y. Luo, K.Y. Zhang, Diffusion and adhesion properties of Cu films on polyimide substrates, Thin Solid Films 473 (2005) 247–251, https://doi.org/10.1016/j.tsf.2004.07.073.

[53] T.Z. Kattamis, On the evaluation of adhesion of coatings by automatic scratch testing, J. Adhes. Sci. Technol. 7 (1993) 783–799, https://doi.org/10.1163/156856193x00439.

[54] M.D. Drory, J.W. Hutchinson, Measurement of the adhesion of a brittle film on a ductile substrate by indentation, Proc. R. Soc. A Math. Phys. Eng. Sci. 452 (1996) 2319–2341, https://doi.org/10.1098/rspa.1996.0124.

[55] A.S.M. Miraz, N. Dhariwal, W.J. Meng, B.R. Ramachandran, C.D. Wick, Development and application of interatomic potentials to study the stability and shear strength of Ti/TiN and Cu/TiN interfaces, Mater. Des. 196 (2020), 109123, https://doi.org/10.1016/j.matdes.2020.109123.

[56] J. Hafner, Ab-initio simulations of materials using VASP: Density-functional theory and beyond, J. Comput. Chem. 29 (2008) 2044–2078, https://doi.org/10.1002/jcc.21057.

[57] J.P. Perdew, K. Burke, M. Ernzerhof, Generalized gradient approximation made simple, Phys. Rev. Lett. 77 (1996) 3865–3868, https://doi.org/10.1103/PhysRevLett.77.3865.

[58] G. Kresse, J. Furthmüller, Efficient iterative schemes for ab initio total-energy calculations using a plane-wave basis set, Phys. Rev. B. 54 (1996) 11169–11186, https://doi.org/10.1103/PhysRevB.54.11169.

[59] H.J. Monkhorst, J.D. Pack, Special points for Brillouin-zone integrations, Phys. Rev. B. 13 (1976) 5188–5192, https://doi.org/10.1103/PhysRevB.13.5188.

[60] K. Abe, Y. Harada, H. Onoda, Study of crystal orientation in Cu film on TiN layered structures, J. Vac. Sci. Technol. B Microelectron. Nanom. Struct. 17 (1999), https://doi.org/10.1116/1.590775, 1464.

[61] K. Abe, Y. Harada, M. Yoshimaru, H. Onoda, Texture and electromigration performance in damascene interconnects formed by reflow sputtered Cu film, J. Vac. Sci. Technol. B Microelectron. Nanom. Struct. 22 (2004) 721, https://doi.org/10.1116/1.1676618.

[62] M. Sekiguchi, H. Sato, T. Harada, R. Etoh, Highly <111> textured Cu film formation on CVD-TiN film by Ti underlayer and Ar sputter etch for damascene interconnection, in: Proc. IEEE 1999 Int. Interconnect Technol. Conf. (Cat. No.99EX247), IEEE, n.d.: pp. 116–118. https://doi.org/10.1109/IITC.1999.787095.

[63] K. Abe, Y. Harada, H. Onoda, Cu crystallographic texture control in Cu/refractory-metal layered structure as interconnects, Appl. Phys. Lett. 71 (1997) 2782–2784, https://doi.org/10.1063/1.120132.

[64] S.L. Shang, W.Y. Wang, B.C. Zhou, Y. Wang, K.A. Darling, L.J. Kecskes, S. N. Mathaudhu, Z.K. Liu, Generalized stacking fault energy, ideal strength and twinnability of dilute Mg-based alloys: A first-principles study of shear deformation, Acta Mater. 67 (2014) 168–180, https://doi.org/10.1016/j.actamat.2013.12.019.

[65] Y.-M. Juan, E. Kaxiras, Generalized stacking fault energy surfaces and dislocation properties of silicon: A first-principles theoretical study, Philos. Mag. A. 74 (1996) 1367–1384, https://doi.org/10.1080/01418619608240729.

[66] C. Brandl, P.M. Derlet, H. Van Swygenhoven, General-stacking-fault energies in highly strained metallic environments: Ab initio calculations, Phys. Rev. B. 76 (2007), 054124, https://doi.org/10.1103/PhysRevB.76.054124.

[67] L. Ma, Y. Lu, S. Li, W. Zuo, Z. Ji, M. Ding, First-principles investigation of Sn9Zn (0 0 0 1)/α-Al2O3 (0 0 0 1) interfacial adhesion, Appl. Surf. Sci. 435 (2018) 863–869, https://doi.org/10.1016/j.apsusc.2017.11.175.

[68] J.R. Davis, Copper and copper alloys, ASM International, 2001.

[69] M. Huang, P.V. Bakharev, Z.-J. Wang, M. Biswal, Z. Yang, S. Jin, B. Wang, H. J. Park, Y. Li, D. Qu, Y. Kwon, X. Chen, S.H. Lee, M.-G. Willinger, W.J. Yoo, Z. Lee, R.S. Ruoff, Large-area single-crystal AB-bilayer and ABA-trilayer graphene grown on a Cu/Ni(111) foil, Nat. Nanotechnol. 15 (2020) 289–295, https://doi.org/10.1038/s41565-019-0622-8.

[70] W.D. Callister, Materials Science and Engineering an Introduction, John Wiley, 2007.

[71] S. Epstein, O. Carlson, The elastic constants of nickel-copper alloy single crystals, Acta Metall. 13 (1965) 487–491, https://doi.org/10.1016/0001-6160(65)90098-2.

[72] P.E. Blöchl, O. Jepsen, O.K. Andersen, Improved tetrahedron method for Brillouin-zone integrations, Phys. Rev. B. 49 (1994) 16223–16233, https://doi.org/10.1103/PhysRevB.49.16223.

[73] A. Adamson, A Textbook of Physical Chemistry, Elsevier, 2012.

[74] L. Pauling, The Nature of the Chemical Bond, Cornell University Press Ithaca, NY, 1960.

[75] W. Tang, E. Sanville, G. Henkelman, A grid-based Bader analysis algorithm without lattice bias, J. Phys. Condens. Matter. 21 (2009), 084204, https://doi.org/10.1088/0953-8984/21/8/084204.

[76] G. Henkelman, A. Arnaldsson, H. Jónsson, A fast and robust algorithm for Bader decomposition of charge density, Comput. Mater. Sci. 36 (2006) 354–360, https://doi.org/10.1016/j.commatsci.2005.04.010.